

Maturity of nearby faults influences seismic hazard from hydraulic fracturing

Maria Kozłowska^{a,1}, Michael R. Brudzinski^a, Paul Friberg^b, Robert J. Skoumal^c, Nicholas D. Baxter^a, and Brian S. Currie^a

^aDepartment of Geology and Environmental Earth Science, Miami University, Oxford, OH 45056; ^bInstrumental Software Technologies, Inc., New Paltz, NY 12561; and ^cEarthquake Science Center, US Geological Survey, Menlo Park, CA 94025

Edited by Paul Segall, Stanford University, Stanford, CA, and approved December 21, 2017 (received for review August 29, 2017)

Understanding the causes of human-induced earthquakes is paramount to reducing societal risk. We investigated five cases of seismicity associated with hydraulic fracturing (HF) in Ohio since 2013 that, because of their isolation from other injection activities, provide an ideal setting for studying the relations between high-pressure injection and earthquakes. Our analysis revealed two distinct groups: (i) deeper earthquakes in the Precambrian basement, with larger magnitudes ($M > 2$), b-values < 1 , and many post-shut-in earthquakes, versus (ii) shallower earthquakes in Paleozoic rocks ~ 400 m below HF, with smaller magnitudes ($M < 1$), b-values > 1.5 , and few post-shut-in earthquakes. Based on geologic history, laboratory experiments, and fault modeling, we interpret the deep seismicity as slip on more mature faults in older crystalline rocks and the shallow seismicity as slip on immature faults in younger sedimentary rocks. This suggests that HF inducing deeper seismicity may pose higher seismic hazards. Wells inducing deeper seismicity produced more water than wells with shallow seismicity, indicating more extensive hydrologic connections outside the target formation, consistent with pore pressure diffusion influencing seismicity. However, for both groups, the 2 to 3 h between onset of HF and seismicity is too short for typical fluid pressure diffusion rates across distances of ~ 1 km and argues for poroelastic stress transfer also having a primary influence on seismicity.

induced seismicity | hydraulic fracturing | frequency-magnitude distribution | b-value | seismic hazard

As the development of unconventional oil and gas resources has become more commonplace, the potential for seismicity induced by wastewater disposal (WD) and hydraulic fracturing (HF) has become an increasingly important issue (1). Recent studies have shown that the extraordinary increase in the number of earthquakes with magnitude (M) ≥ 3 in the central and eastern United States over the past decade is largely a result of large increases in the amount of wastewater disposal (2–4). Based on these studies, there is a growing tendency to consider WD operations as the primary concern in the assessment of induced-seismicity hazards (5, 6). Moreover, these findings have been taken as evidence for the physical model where fluid injection increases pore fluid pressure, lowering the effective stress on faults and promoting seismic slip. However, a growing number of studies have found evidence that HF alone is also responsible for $M \geq 3$ seismicity (7–9) although a given HF well has shown lower prevalence of inducing $M \geq 3$ seismicity than a WD well (10, 11). While it is plausible that the rapid changes in pore fluid pressure are inducing slip on adjacent faults (12), it is unclear whether appropriate permeability structures exist for rapid transmission of pore fluid pressures (9). Some recent research suggests that poroelastic stress could have a larger influence on seismicity than pore fluid perturbations in cases of both WD and HF (13–16), but others contend that poroelastic stress dissipates too quickly from the injection interval (17). However, these studies seeking to discern between these mechanisms are either strictly theoretical or target only a single observed sequence.

In this study, we focused on the easternmost part of Ohio, Harrison County, where HF began to target the unconventional Utica/Point Pleasant tight shale formations in 2012. This area had essentially no documented seismicity before 2010 (Fig. 1) but has since had over a dozen cases of induced seismicity. The first large sequence occurred in 2011, when WD induced hundreds of events $M > 1$ up to a maximum observed magnitude (M_{MAX}) 4.0 in Youngstown (18, 19). Since then, seismicity associated with WD has also been observed in Trumbull County (M_{MAX} 2.1) (20) and Washington Counties (M_{MAX} 3.1) (10) whereas seismicity associated with HF has occurred in Poland Township (M_{MAX} 3.0) (9), Belmont and Guernsey Counties (M_{MAX} 2.6) (10), and Harrison County (M_{MAX} 2.6) (21, 22). The seismicity associated with HF has been most frequent in Harrison County, where it was first recorded in October 2013. The relatively slow rate of well drilling and HF stimulation relative to other shale plays, as well as the lack of nearby WD wells, makes this area an ideal setting for isolating the relationships between high pressure injection and induced seismicity. To detect and locate additional seismic events induced by ongoing HF in the area, the Division of Oil and Gas Resources Management at the Ohio Department of Natural Resources (ODNR) deployed four portable short-period three-component seismometers in Harrison County by November 2013. By the end of 2015, another four major sequences of seismicity were detected using the repeating signal detector (RSD) algorithm (22). The preliminary hypocenters determined in that study suggested that the seismicity occurred

Significance

Recent studies have focused on how wastewater disposal wells have caused dramatic increases in eastern US earthquakes. We focused instead on less common cases where hydraulic fracturing alone has caused earthquakes and found seismicity separated into two depth zones: a shallow zone on younger faults, with more small-magnitude earthquakes than expected, and a deeper zone on older faults, with larger magnitude earthquakes and seismicity continuing after fracturing stops. Hence, inducing deeper seismicity creates more hazard. Our observations are consistent with prior geologic, laboratory, and theoretical work indicating that age and maturity of faults causes the different seismicity patterns. We utilize data from well operators to demonstrate that both fluid pressure changes and rock stress transfer are needed to explain our observations.

Author contributions: M.K. and M.R.B. designed research; M.K. and M.R.B. performed research; P.F. contributed new reagents/analytic tools; M.K., P.F., R.J.S., and N.D.B. analyzed data; and M.K., M.R.B., and B.S.C. wrote the paper.

The authors declare no conflict of interest.

This article is a PNAS Direct Submission.

Published under the PNAS license.

¹To whom correspondence should be addressed. Email: mkozlow@igf.edu.pl.

This article contains supporting information online at www.pnas.org/lookup/suppl/doi:10.1073/pnas.1715284115/-DCSupplemental.

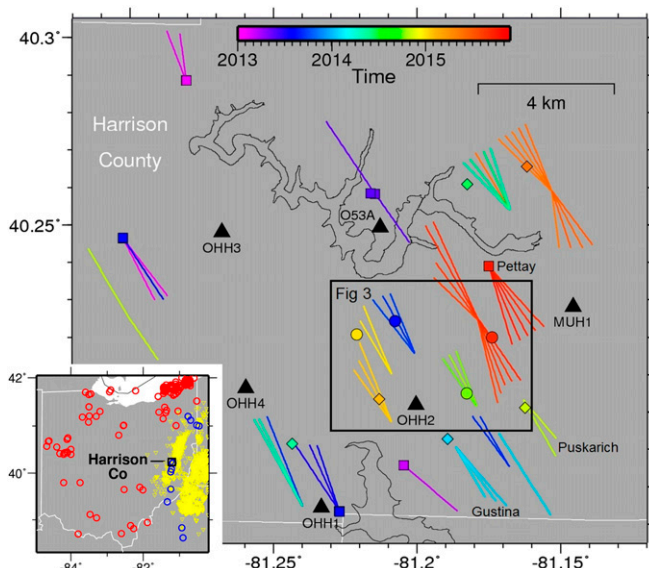


Fig. 1. Map of southwestern Harrison County, Ohio, showing the results from RSD processing (22). Lines show locations of unconventional well head and toe, colored by time of HF, restricted to the time range of the RSD analysis. Triangles show seismic stations used in this study. Symbols are also colored by time and show locations of the strongest events from major (>750 events, circles) and minor (<750 events, diamonds) earthquake sequences determined by Skoumal et al. (22). Squares mark well heads where stimulation occurred before the local network was installed, but HF correlates temporally with seismic activity and S-wave minus P-wave ($S - P$) times recorded by O53A are consistent with earthquakes occurring near these wells. (*Inset*) Map of Ohio showing earthquakes before 2010 (red), HF wells (yellow), and induced seismicity (blue) (20, 30). Square marks location of larger map.

beneath or near the wells that were active at the same time, but a detailed relative location study has not yet been performed. Of particular interest is whether the different wells are stimulating seismicity on a larger fault that extends across the entire region or whether the seismicity occurs on separate smaller faults. Distinguishing between these scenarios is necessary to estimate the maximum magnitude potential and resulting hazard these events pose, and our study is specifically designed to provide the detailed location analysis for this purpose.

Another key component for evaluating the hazard associated with induced seismicity is to determine the frequency-magnitude distribution (FMD). The FMD for a given earthquake's population describes the rate of earthquakes across all observed magnitudes, which is critical for estimating the likelihood of larger and potentially damaging earthquakes from an initial set of smaller events (23). The Gutenberg and Richter (24) relation (G-R) defines FMD as $\log_{10}N(M) = a - bM$, where N is the cumulative number of earthquakes of magnitude $\geq M$, and a and b (the so-called b-value) denote constants characterizing an earthquake population's specifics. As in many self-similar distributions in nature, there is evidence for a long-term constant and universal b-value of 1 (25–27). However, deviations from this value are thought to represent a wide range of physical phenomena (28, 29). However, the ultimate importance of characterizing b-values is that it is necessary to forecast the likelihood of larger events. For example, lower b-values indicate more larger events relative to a typical population and hence a larger hazard.

Finally, the depth of fluid injection operations has been suggested to influence the hazard from induced seismicity (30–32). Based on the observational correlations and geomechanical and hydrologic modeling in these studies, the likelihood of induced seismicity is higher the closer the WD or HF operations are to the Precambrian crystalline basement rocks. The suggested reasoning is that the

faults in these older rocks are more capable of producing seismicity of sufficient magnitudes to be detected ($M > 2$) and potentially hazardous [modified Mercalli intensity scale ($MMI \geq V$)].

In this study, we performed a detailed investigation of the largest seismic sequences associated with HF in Harrison County, Ohio, from 2013 to 2015. To better understand the causes of this seismicity, we utilized improved estimation of event detection, hypocentral locations, frequency-magnitude distributions, and focal mechanism determinations in conjunction with detailed operational and production information. We found that the seismicity induced by HF falls into two groups that reveal important differences in fault maturity with depth. These differences influence the seismic productivity both during and after HF, which indicates that wells inducing deeper events pose significantly larger hazards. Moreover, the eventual water and hydrocarbon production of these wells is correlated with the type of seismicity they produce, providing clues about the extent of stimulation. Finally, the temporal-spatial relationship between HF and seismicity requires triggering mechanisms faster than pore fluid pressure diffusion.

Results

Spatial Patterns of Seismicity. Fig. 2 shows our relocated epicenters colored according to the associated HF well. The epicenters outline several east–west-oriented trends, similar to that seen in other cases of induced seismicity in Ohio (10). The maximum horizontal stress (S_{Hmax}) is oriented northeast–southwest in eastern Ohio (33, 34), as demonstrated by well lateral trajectories oriented perpendicular to S_{Hmax} to facilitate fracture opening (Fig. 2). The apparent east–west fault orientations from seismicity are $\sim 30^\circ$ from S_{Hmax} and optimally oriented for shear slip reactivation. The lengths of the bands of seismicity appear to be ~ 1 km or less as the refined relative locations provide evidence that seismicity is not occurring on a single through-going fault. However, there appear to be two cases (Ryser–Davidson and Tarbert–Hamilton) when HF ~ 1 y later induced seismicity on the same fault activated earlier. Fault lengths limited to 1 km are similar to all previous induced seismicity in Ohio, but this represents the imaging of a multitracced network of faults being induced by multiple HF well pads in the United States.

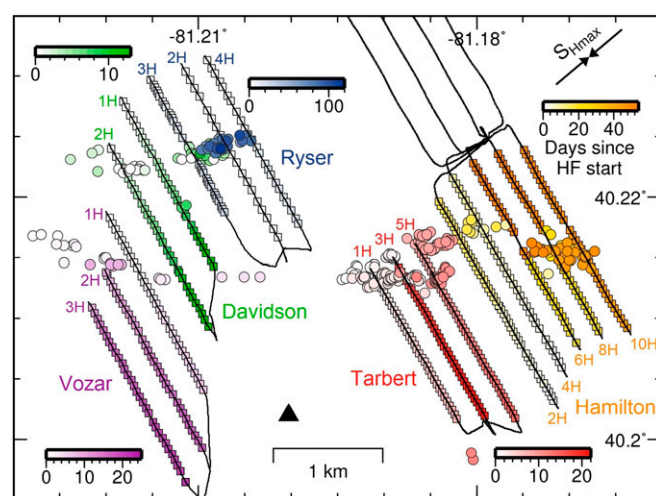


Fig. 2. Map showing five major sequences in Harrison County from 2013 to 2015 analyzed in this study. Curved lines indicate horizontal well drill paths. Stimulation stages (squares) and double-difference relocated seismicity (circles) are shaded using a time scale since the start of HF, with a different color for each well pad. Circle diameter shows mean horizontal location uncertainty. Nearest seismic station is shown as a triangle.

Another key feature is that seismicity tends to occur within or very near the footprint of the well pad to which the seismicity is temporally correlated (Fig. 2). The footprint size is based on the extent of varying numbers of horizontal well laterals (1H to 10H).

Fig. 3 shows the calculated 3D separations between seismicity and the most recent HF stages (squares, Fig. 2). These values vary from 140 to 1,220 m, similar to the Poland Township case, where only certain stages within 800 m of the fault induced seismicity (9).

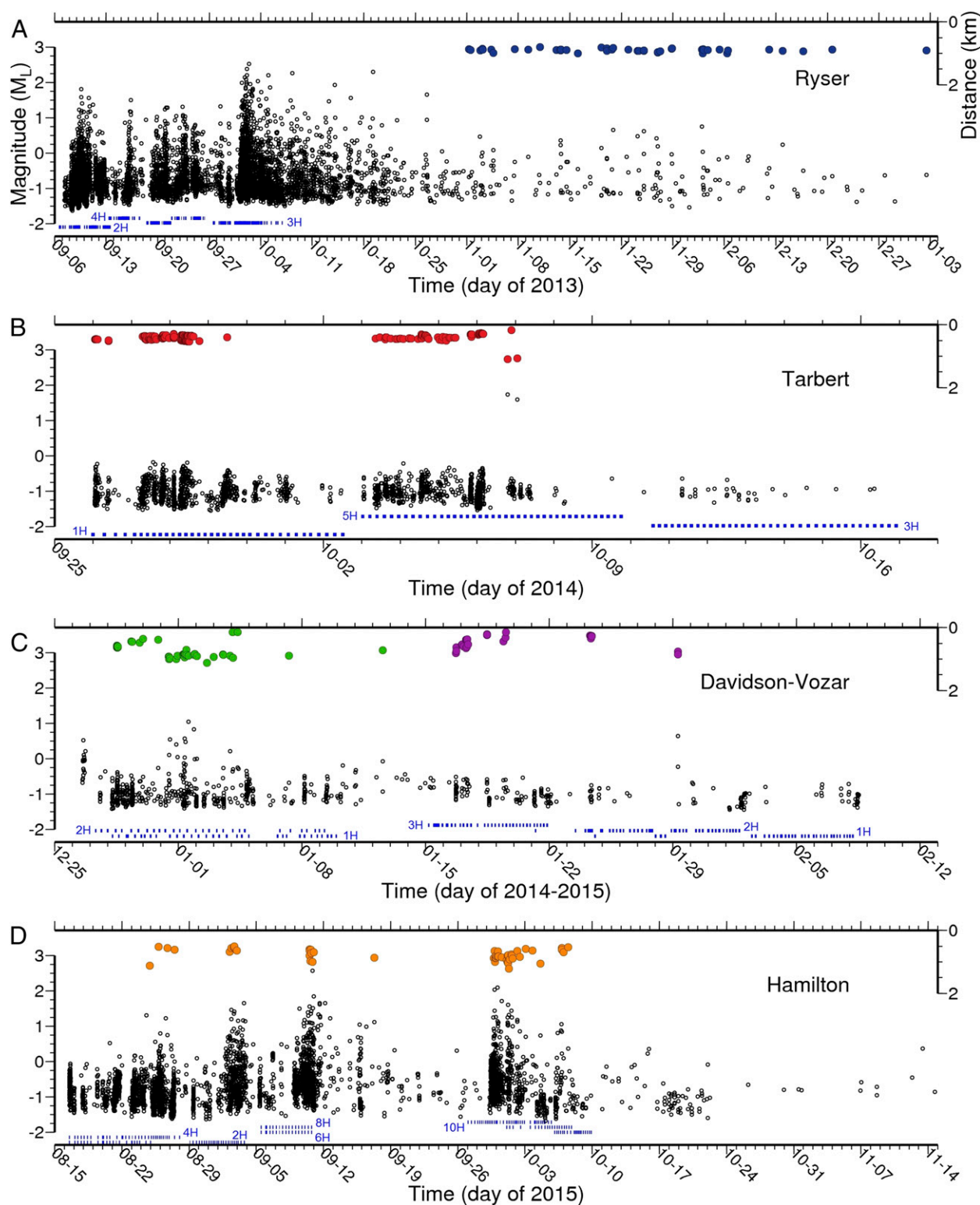


Fig. 3. Temporal distribution of seismicity detected using RSD, showing magnitudes of seismic events (black) together with HF stages labeled with individual well names (bottom blue bars), shown for all studied wells (A–D). Top colored circles show 3D distance from each located earthquake to nearest HF stage that occurred before the earthquake. Well locations and colors correspond to those in Fig. 2.

Cross-sections through the double difference relocations revealed a key finding that seismicity is separated into two different depths (Fig. 4). The previous work in Youngstown, Poland Township, and Trumbull County (19, 9, 20), as well as work on the Ryser pad seismicity in Harrison County (21), found that induced seismicity occurred in the crystalline Precambrian rocks of the uppermost basement. Our analysis found that nearly all of the locatable Ryser and Hamilton pad seismicity occurred in the uppermost basement (Fig. 4), consistent with the earlier findings. The basement depth is well-determined in Ohio based on an integrated study of multiple data sources (35). We also found that over half of the Davidson seismicity occurred in the uppermost basement, very near the Ryser seismicity (Fig. 4). However, the remaining Davidson seismicity occurred significantly above the basement, closer to but still below the target Utica–Point Pleasant formations. Seismicity associated with the Vozar well pad also occurred at shallower depths. Nearly all of the Tarbert seismicity was also at similar shallow depths, except for the two notably larger ($M \sim 2$) events. Utilizing the clue that the two larger Tarbert events occurred deeper than the other Tarbert events, we also noted that the deeper seismicity associated with the Ryser and Hamilton pads included more large events than the shallower seismicity associated with the Davidson and Vozar pads.

Temporal Patterns of Seismicity. Fig. 3 shows the timing of HF stages for the five multiple-lateral well pads associated with the largest seismic sequences. The onset of seismicity was well correlated with the onset of HF at these wells. Not all well pads have detailed (minute precision), publicly available stimulation reports, but there are two well pads with this level of detail and no other well pads with HF in close proximity in the days before the onset of HF. For the Ryser well pad, there were only 120 min from the initiation of HF to the onset of seismicity, and for the Davidson well pad the time offset was 171 min. For comparison, the Poland Township case a few counties away only had seismicity during a subset of stages (9), but it appears the time offset was 109 min based on the correlation between HF and seismicity.

In general, seismicity was well-correlated with the onset of HF for all well pads, and there were distinct bursts of seismicity that correlated with individual stages of HF (Fig. 3). However, the seismicity only halted at shut-in for the Tarbert and Vozar well pads. Seismicity continued in the same general locations for over a month after the Ryser and Hamilton pads shut-in although the

operations at the nearby Pettay pad following the Hamilton pad created some level of uncertainty in that case. This seismicity that continues after shut-in occurred at lower seismicity rates than during HF and decayed over time (*Supporting Information*), but the magnitude ranges were similar to that during HF. For this reason, we believe that there is a distinctly different pattern of seismicity following the Tarbert and Vozar HF and the lack of seismicity after shut-in of those well pads was not due to lack of detection. It is important to note that the occurrence of seismicity did not influence the HF operations except for Hamilton, where communication between the operator and regulator resulted in stimulation being halted on well laterals 6H and 8H (Fig. 2) for over 2 wk following the strongest earthquake and the injection pressures and volumes were decreased afterward.

Frequency-Magnitude Distribution. To better understand the magnitude differences between the two depth groups, we estimated FMDs for each sequence and compared them with typical G–R relations (Table S1). The FMDs differed for the two separate depth zones: the deeper sequences associated with the Hamilton and Ryser wells had overall low b-values (0.72 and 0.76) and the shallower sequences from the Tarbert and Vozar wells had high values (1.54 and 1.91). The Davidson well sequence, which consisted of two clusters differing in depths, showed a b-value (1.3) in between that of the two clusters. Similar large variation of b-values were reported for different cases of HF-induced seismicity, typically ranging from 0.8 to 1.0 for out-of-zone seismicity that reaches larger magnitudes (21, 9) to 2.0 for smaller near-target microseismic events (36–38). Comparing b-values between different studies can be difficult as authors often use different types of magnitudes and different techniques for magnitude of completeness (M_c) estimation, both influencing the b-value. Since our study area was relatively small and we detected all events using the same station and the same approach, it is legitimate to compare the obtained b-values and to associate their variation with geological or operational factors.

To look for any temporal changes of b-value like those seen in the study of WD in Youngstown (19), Fig. 5 separates the catalogs into an early, late, and post-HF phases (if it existed). For all sequences except Tarbert, the b-value was highest in the early phase. For the deeper Ryser and Hamilton seismicity, the b-value was slightly higher (~ 0.9) initially, but decreased during stimulation to values (~ 0.7) that are similar to those of seismicity induced by WD in Ohio (10, 19, 20). Authors analyzing b-value

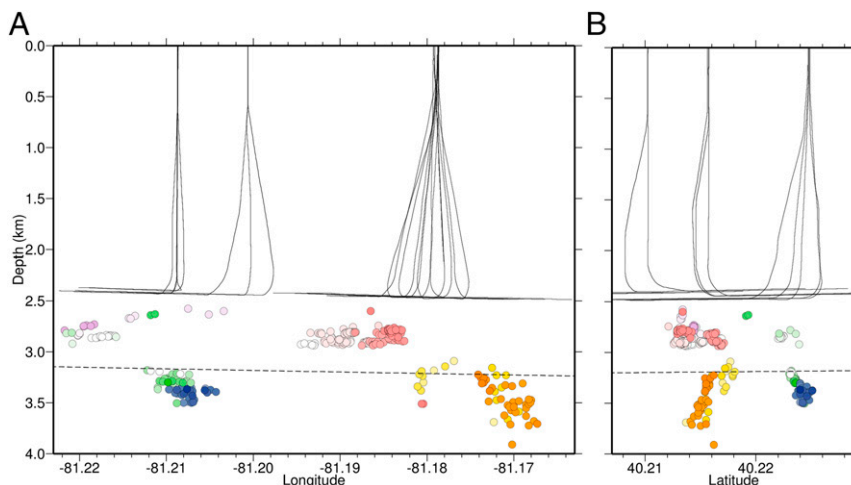


Fig. 4. Cross-sections taken (A) east–west and (B) north–south through the relocated seismicity shown in Fig. 2. Colors correspond to those in Fig. 2. Circle diameter shows mean vertical location uncertainty in our study. Curved lines are well lateral drill paths. Dashed line marks the top of the Precambrian basement rocks (35).

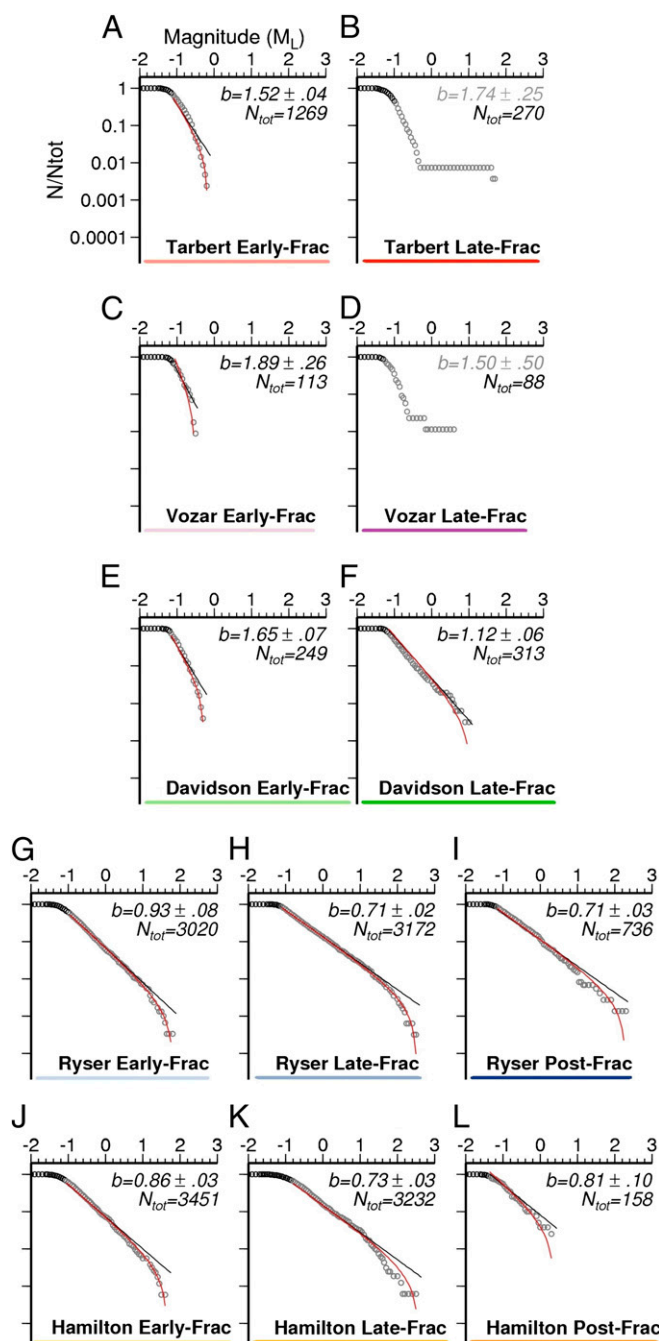


Fig. 5. Frequency-magnitude distributions of five detected seismic sequences, divided into HF phases (A–L). N/N_{tot} is the number of events at or above a given magnitude divided by the total number of events. Colors follow color scale in Fig. 2. The black circles are below the estimated M_c . b -values were calculated using maximum-likelihood estimate, and uncertainties were estimated using bootstrap resampling. The black line represents maximum-likelihood G–R fit, and red curves represent truncated G–R fit. Please note that Tarbert and Vozar Late Frac seismicity (B and D) do not obey log–log power law distribution.

variations in areas where underground fluid injection is performed associate changes in the parameter with changes of pressure gradient (29, 39). While most wells showed a gradual decrease over time, the Davidson case showed a larger change that corresponds to a change in depth. The early phase had shallower seismicity and high b -values (1.65) while the late phase had deeper seismicity and lower b -values (1.12). Closer exami-

nation of the Tarbert exception reveals that the late phase FMD did not follow a log–log power law relationship due to a few much larger events (Figs. 3 and 5). The late phase for Vozar showed this pattern to a lesser degree, and a similar trend was observed for the Trumbull and Youngstown WD wells (20).

The FMDs of several phases of seismicity appeared to be truncated with a curvature that produces fewer larger events relative to what is expected for a linear G–R (power law) FMD similar to that of Huang and Beroza (40). For each phase of seismicity, we used an F-ratio test to determine the confidence level associated with improved fit of a truncated form of the G–R curve (41, 42) over the linear G–R, taking into account the extra degree of freedom. For later phases of Tarbert and Vozar, FMDs did not follow a linear G–R or truncated G–R, but they appear to be similar to a nonlinear trend observed for the Trumbull and Youngstown WD wells (10). For Davidson Late and Hamilton Post, the linear G–R fit was better than the truncated G–R. For Vozar Early, truncated G–R was a better fit at 98% confidence. For all other cases, truncated G–R was a superior fit at >99.999% confidence.

Focal Mechanism and Waveforms Similarity Analysis. Due to limited number of local stations, we were only able to calculate a focal mechanism for the two strongest ($M > 2.5$) events from Ryser and Hamilton sequences that were well-recorded on regional stations; their focal mechanisms are presented in Friberg et al. (21) and Fig. S2, respectively. Both focal mechanisms are similar and consistent with those determined for strongest events in Youngstown (18) and Poland Township (9), showing similar east–west faults orientation as the hypocentral distribution. All mentioned events were located within the Precambrian basement, suggesting that a fault network with parallel traces that is optimally oriented exists across eastern Ohio.

Unfortunately, none of the shallower earthquakes were large enough to determine a focal mechanism. Their proximity to the target formation and high b -values might suggest they occurred via a similar process to that of operationally induced microseismicity, which is thought to represent creation of new, or opening of preexisting, fractures and hence have a non–double-couple focal mechanism representing their tensile character (43). However, the detection tool used to create the events we analyzed was based on high waveform similarity, which should retrieve events with similar focal mechanisms. Visual comparison of first-motion polarities for deep and shallow events confirmed the similarity (Fig. S3). HF-generated fracture orientations are usually different from preexisting fault orientations (44). Moreover, Wolhart et al. (44) illustrates how typical shale fracturing events occur at $M < -2$ and that larger events represent reactivation of slip on preexisting faults outside the target formation. Together, these findings suggest that the shallow seismicity that we observed represents on-fault slip rather than a fracturing process and that both Precambrian and Paleozoic faults experience a common faulting regime.

Operational Data from HF Wells. To look for any patterns in injection parameters that correlate with the depth and b -value patterns we observed, we used individual stage values listed in stimulation reports to calculate mean (Table S2) and maximum (Table S3) injection pressures and volumes. We also examined values from three neighboring well pads (Pettay, Gustina, and Puskarich) (Fig. 1) with HF in our study period but with only very weak seismicity (22). The injection parameters did not correlate with the depth and FMD patterns we observed. Ryser and Hamilton had slightly higher breakdown pressures than Vozar and Tarbert (Tables S2 and S3), but these variations are similar to that observed at wells with only weak seismicity, indicating no clear relationship between injection parameters and seismicity.

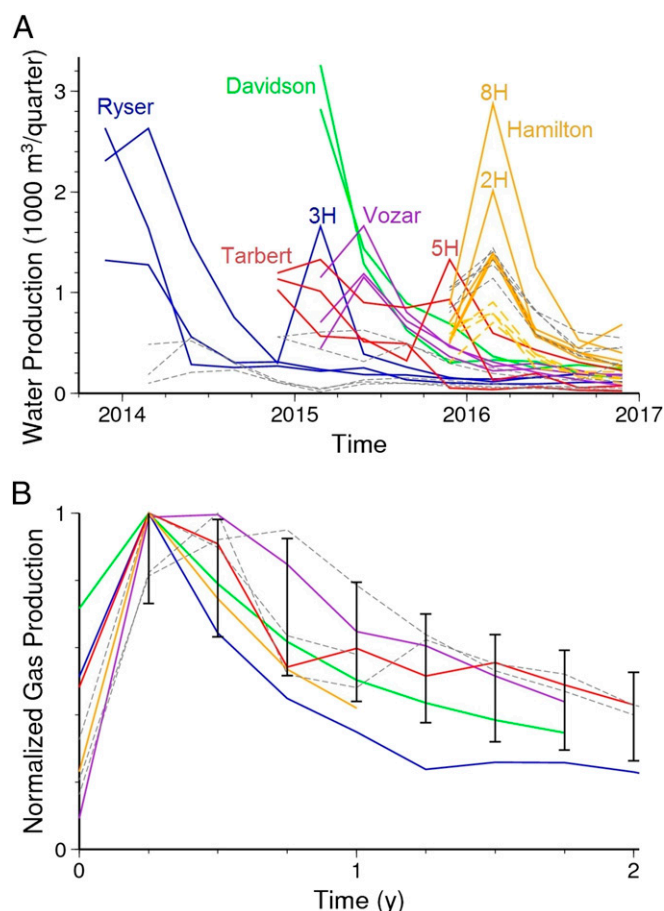


Fig. 6. Quarterly production data from five wells with seismicity we analyzed (colored lines). Gray lines show data from three other well pads with HF during our study with only weak seismicity. (A) Water production. (B) Natural gas production aligned on the first production quarter, normalized to the largest value. Error bars show the SD for all 269 wells in Harrison County.

We also analyzed water and gas production data reported to ODNr quarterly for the five wells with seismicity to look for other clues about what led to the two groups of seismicity (Fig. 6). For comparison, we again included data from wells with little seismic activity: Pettay, Puskarich, and Gustina. The wells with deep seismicity (blue, green, and yellow curves in Fig. 6) showed higher values of water production over the first few quarters than the wells with shallow (purple and red) or no seismicity (dashed gray). Water production typically fell off over time (Fig. 6A), but the Ryser well lateral closest to the Davidson wells (3H) saw an unexpected increase during HF of the Davidson wells (green lines). This is one of the few times when seismicity during HF of one well pad aligned with seismicity during HF of a later well pad (Fig. 2). The other time seismicity appeared to align was for the Tarbert and Hamilton wells, and a similar increase in water production occurred for the nearest Tarbert well lateral (5H) during HF of the Hamilton wells (e.g., 8H and 2H). Water production is often correlated with gas production, but the wells with deep seismicity did not have larger gas production (Fig. S4) so it cannot explain the patterns. For example, the Ryser well had one of the largest initial gas production values, but it was similar to two wells with weak seismicity. However, if we plot the gas production aligned on the start time with values normalized (Fig. 6B), wells with deep seismicity have production values that fall off faster (lower normalized values at later times, particularly

after 1 y) than the wells with shallow or no seismicity. We hypothesize that the fracturing and propping process appears to be less effective for wells that induce deep seismicity due to more extensive hydrologic connections outside the target reservoir.

Discussion

Our observations indicate that there is a network of preexisting, critically stressed faults in this area before HF, primarily based on the rapid onset of optimally oriented seismicity once HF begins. The relocated seismicity indicates that preexisting faults occur both in the Precambrian and the Paleozoic section. We hypothesize that both the Paleozoic and Precambrian seismicity occur on left-lateral strike-slip faults that are optimally oriented relative to S_{Hmax} . While the hypocenters do not illustrate a full connection between the two depth zones, we hypothesize a connection via linked, high-angle fault systems that originate in the master fault in the crystalline basement and extend upward through or near to the target Utica–Point Pleasant reservoir interval. Strike-slip systems experiencing convergence, as appears to be the case based on focal mechanisms and proximity to the Appalachian orogenic belt, are expected to develop a positive flower structure (45). Evidence for this geometry was recently found ~100 km south in Washington County through combined analysis of seismicity and mapping the subsurface structure in a case of WD-induced seismicity (46).

Fig. 7 shows seismic rupture areas as circles synthetically computed from the average FMDs for the Paleozoic and Precambrian seismicity groups to visually illustrate the differences in b-value and maximum magnitudes. The high b-value of the shallow seismicity (1.75) results from so many small events that the fault patch appears to be full of similar sized seismicity whereas the low b-value of the deep seismicity (0.75) is caused by

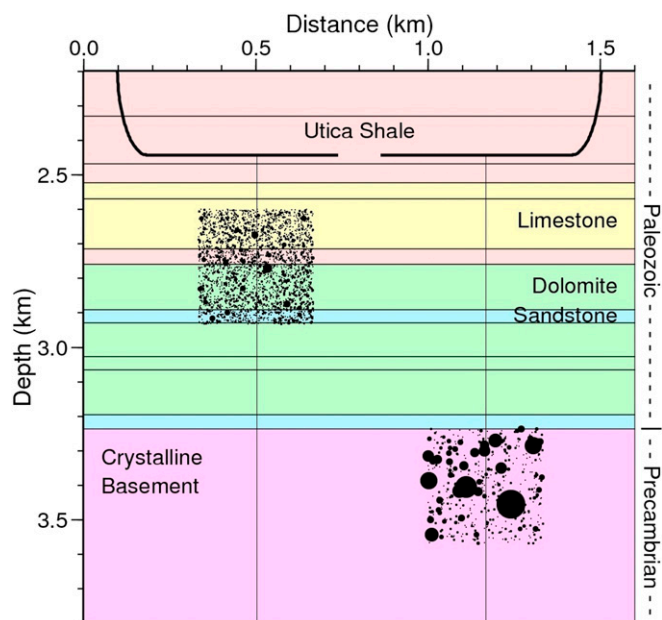


Fig. 7. Schematic cross-section illustrating differences between the shallow seismicity in the Paleozoic sedimentary rocks and the deep seismicity in the Precambrian basement rocks. Circles show seismic rupture areas synthetically computed from the average FMDs, utilizing a magnitude to circular slip area approximation (81), but with a low stress drop [0.1 MPa (megapascals)] to produce visible circle sizes. Circle locations are randomly assigned in a square area in the depth range observed. The minimum size plotted ($M > -1$) is from our average M_c . Strata are colored by predominant rock type, with depths estimated from the closest deep well logs. Curved lines show example well paths.

more magnitude variability and larger events visually dominate the fault patch. Efforts to understand high *b*-values of operationally induced microseismicity recently led to the idea that mechanical bed thickness in the target formation limits the length of fractures (47, 48). However, waveform and first motion similarity between Paleozoic and Precambrian seismicity indicates that the high *b*-values of our Paleozoic seismicity are not associated with the fracturing process (Fig. S3). Moreover, this seismicity occurs ~400 m below the target formation, straddling several different types of strata (Figs. 4 and 7), with magnitudes larger than any operationally induced microseismicity (49).

We interpret that the difference in *b*-values for shallow versus deep seismicity is due to differences in fault maturity based on the different age of the rocks that host the faults (~450 My for Paleozoic; ~1 Gy for Precambrian). Recent laboratory stick-slip experiments revealed that the acoustic emission events produced on rough, fractured surfaces have much higher *b*-value (1.2) than those on smooth, polished surfaces (0.7) (50). These results suggest that more mature faults develop smoother surfaces with broader spatial areas of homogeneous stress that promote larger ruptures, leading to lower *b*-values, whereas younger faults are associated with rougher surfaces and stress field heterogeneities that have narrower spatial extent, leading to smaller rupture sizes and higher *b*-values. Studies have also found that the size of seismic asperities increases with increasing fault maturity (51), as more slip on more mature faults appears to reduce the fault roughness (52). Laboratory studies suggest that increasing strain localization is an important part of this process (53). Depth dependence of *b*-values was also observed for seismicity in California (54), where the changes were attributed to greater heterogeneity of shallow formations and smaller lithostatic stress in comparison with deeper formations. However, that study analyzed a much greater depth range (15 km) than the one in this study (1.5 km), such that stress variations are unlikely to be responsible for the vastly different *b*-values in our study. We cannot rule out that material property changes between the crystalline basement and sedimentary rocks are contributing to the differences in seismicity, but we find no studies proposing or documenting different *b*-values due to material properties. The maturity difference hypothesis is also justified from a geological point of view.

Subsurface mapping of Paleozoic stratigraphic units in conjunction with limited seismic reflection data indicate that basement-involved faults in eastern Ohio have experienced multiple periods of deformation throughout the Paleozoic. In Harrison County, both NW–SE and E–W trending fault zones display Cambrian-aged extensional deformation, followed by Pennsylvanian–Permian transpressional reactivation (55). Throughout southeastern Ohio, similar faults are associated with variable thickness trends in Cambrian, Silurian, Devonian, and Pennsylvanian strata, suggesting that multiple episodes of reactivation throughout the Paleozoic developed along zones of weakness in the Precambrian crystalline basement (55–59). Given this history, associated fault zones would be significantly more mature lower in the stratigraphic section, with the highest degree of maturity in the Precambrian crystalline basement. It is also important to note that these faults are observed extending from the Precambrian basement into the overlying Paleozoic section, commonly tipping out in Upper Ordovician–Devonian strata (55, 57–59). As such, these faults and associated fracture zones may provide permeability pathways from hydraulic-fracturing targets in the Ordovician Utica–Point Pleasant reservoir into the Lower Paleozoic sedimentary strata and underlying Precambrian crystalline basement.

The seismicity we detected occurred rapidly after the onset of HF (120–171 min). While we don't know the exact location of the first seismic event in the Ryser, since the local network was installed several weeks later, the O53A waveform similarity in-

dicates that it occurred in the same group as those located with the network. Based on this, there is ~1,200 m between the first stage at the Ryser well and the first earthquake. We can be more precise for Davidson, where the first stage is separated by 820 m from the first earthquake. For a saturated homogeneous medium, these values correspond to hydraulic diffusivities of 18 m²/s and 5.2 m²/s, respectively, which are more than an order of magnitude larger than other estimates of diffusion-triggered seismicity in shallow fault zones and induced seismicity (60, 61). This observation is more consistent with recent research that has suggested that poroelastic stress could have a larger influence on seismicity than pore fluid pressure changes in cases of both WD and HF (13–15). In particular, Deng et al. (14), discussing a case of HF in Canada, found that the effect of poroelastic stress transfer was large enough to induce seismicity even at distances >1 km from a single well. In our case, this mechanism appears to play a role throughout HF as many different stages along the horizontal well that extend over a kilometer continue to trigger seismicity on the same fault. This would be difficult to achieve with pore fluid pressure changes alone as each spatially separated stage would need to create fluid pathways that connect to the same fault. Moreover, we do not see an increasing trend in distance from the stage to the seismicity over time (Fig. 3) that would otherwise be expected if pore pressure diffusion were the sole cause. In addition, the strong temporal variations in injection associated with HF are more likely to cause poroelastic stress changes (13, 16).

While Deng et al. (14) argued that poroelastic stresses are the dominant factor responsible for a sequence of earthquakes $M \geq 2$ during HF, most studies have argued that pore fluid pressure changes are the dominant factor inducing seismic events in cases of HF (39, 62, 63), and our study finds evidence for this process as well. Foremost, water production increases in neighboring wells when induced seismicity occurs (Fig. 6A) while we do not observe a similar jump in gas production (Fig. S4). If poroelastic stress was increasing pressure near the well, it should increase both water and gas production. Instead, the increased water production indicates more hydraulic conductivity that should enable pore fluid pressure changes outside the shale target. Likewise, the decrease in *b*-values over the course of HF for wells that induced deep seismicity (Fig. 5 G, H, J, and K) suggest that pore fluid pressures may increase in these fault zones during the HF. This is based on studies showing that increased pore fluid pressure, caused either by natural processes in the production zone or by high pressure fluid injection, results in lowered effective normal stress and decreased seismicity *b*-value (29, 64–66).

The truncation of the FMD during HF (Fig. 5 A, C, E, G, H, and J) also indicates the effect of pore fluid pressure on seismicity as injection progresses. A truncated FMD was found for a detailed study of wastewater disposal-induced seismicity along the Guy–Greenbrier Fault in Arkansas (40). In that study, the sum of injection wastewater volumes provided a good constraint on the seismic moment using the relationship of McGarr (67), consistent with the idea that the finite size of the medium stimulated by fluid injection limited earthquake source volumes (68). So, while most studies have concluded that either pore fluid pressure changes or poroelastic stress transfer is the dominant factor for inducing seismicity, we believe our study demonstrates that both mechanisms are necessary to explain the observations. Intriguingly, the Ryser and Hamilton cases with post-shut-in seismicity show the *b*-value rebounding and the FMD moving from truncated G–R to linear G–R during the post-HF time period (Fig. 5).

This matches the pattern seen by Huang and Beroza (40) after the termination of wastewater disposal injections, where seismicity continued even after the earthquakes stopped migrating along the Guy–Greenbrier Fault. This observation matches

conclusions made by Segall and Lu (13) that postinjection earthquakes are triggered by continuously increased Coulomb stress away from the injection point. The process of stress relaxation, featured by diffused and persistent seismicity, follows Dieterich's seismicity rate model (69). The absence of post-shut-in seismicity for the Paleozoic seismicity in our study is similar to observational studies of aftershocks along shallow faults that found sedimentary rocks do not host aftershocks at magnitudes we can record (70, 71). The limited aftershocks were interpreted to be due to different rheological and frictional behavior of sedimentary rocks relative to metamorphic or igneous rocks. Subsequent modeling of seismogenic faults with damage rheology found that lower effective viscosity of sedimentary rocks could reproduce the paucity of aftershocks (72). Laboratory measurements of shales and sands have shown time-dependent viscous behavior such that differential stress changes would be dissipated over time scales on the order of days (73, 74). This supports the notion that the differential stress caused by induced earthquakes is relaxed rapidly in the Paleozoic section due to the lower effective viscosity of sedimentary rocks.

Our results suggest that the seismic hazards associated with HF are largest when Precambrian faults are being activated. The maturity of these faults appears to allow larger ruptures and a greater ratio of larger to smaller magnitudes. Seismicity also extends longer after injection, apparently due to slower stress relaxation in basement rocks. In contrast, less mature faults and weaker rock layers in the Paleozoic appear to limit magnitudes and post-shut-in activity. Seismicity in our study area has not yet reached M3, but this may be fortuitous considering the total volume injected at the well pads ranges from 0.48 to 1.74×10^6 barrels (bbl), with the largest being 3.5 times the volume injected at the Youngstown WD well that produced an M4.0 earthquake. The relationship between injected volume and moment magnitude of McGarr (67) indicates that the maximum magnitude for these well pads would be moment magnitude (M_w) 4.2 to M_w 4.5. There have been several $M > 4$ earthquakes induced by HF in remote Alberta, Canada, with local magnitude (M_L) 4.4 to M_L 4.8 and M_w 3.9 to M_w 4.1 (11, 62), so there does not appear to be a limitation based on the HF process. Detailed analysis of the first $M \approx 4$ case in Alberta found that the largest event occurred in the basement, ~700 m below the target formation (63). A recent M_L 3.7 earthquake on June 3, 2017, occurred ~30 km south of our study region in proximity to active HF and was preliminarily located in the Precambrian (geosurvey.ohiodnr.gov/quakes-2010-to-present-pgs/batesville-june-03-2017), which supports the notion that HF can induced $M \approx 4$ earthquakes in Eastern Ohio, raising the likelihood of a damaging event.

Materials and Methods

Seismic Data. All analyzed earthquakes were detected using the RSD algorithm (22) using an excellent EarthScope station (O53A). Relocations of the strongest of detected events are possible due to the deployment of local stations. Four short-period, three-component sensors were deployed by ODNR (OHH1, OHH2, OHH3, and OHH4) in October 2013, but two of them were moved to other areas of Ohio in May 2014. In September 2015, a

broadband seismometer was deployed further east to enclose the seismicity by Miami University (MUH1) (Fig. 1).

Hypocentral Location. Our location analysis followed the approach of previous work in Youngstown (19), Poland Township (9), and Trumbull County (20), Ohio using *elocate* (75) to establish a catalog of location for all matched events and *hypodd* (76) to refine the relative locations (see [Supporting Information](#) for more detailed discussion of the procedure and resulting uncertainties). We have tested multiple velocity models to specifically verify the depth distribution of analyzed events, but having at least one station within an epicentral distance less than the focal depth from all analyzed sequences plays a major role in constraining the hypocentral depths with low uncertainty (77).

Earthquake FMD. The initial earthquake catalog of origin times and Richter magnitudes is from the enhanced repeating seismicity detector of Skoumal et al. (22). We focused on the four major seismicity sequences with at least 700 events (Fig. 3), but one case consisted of two spatially separate clusters associated with the Davidson and Vozar wells. We calculated FMDs of these five seismic sequences (Fig. 5), following the Gutenberg–Richter b-value estimation of Bender (78):

$$b = 1 / [\ln(10) \times (M_{\text{avg}} - (M_c - M_{\text{bin}}/2))]$$

where M_{avg} is the sampling average of the magnitudes, M_c is the magnitude of completeness, and M_{bin} is the bin size of earthquake magnitudes. M_c was determined using the maximum curvature algorithm (79). The results for each sequence are listed in [Table S1](#). Uncertainties were estimated using bootstrap resampling (Fig. 5 and [Table S1](#)). The mean difference from uncertainties calculated with the method of Aki (42) is <0.01 . To calculate the truncated G–R fit, we used the equation of Caputo (41). We then used an F-ratio test to determine the confidence level associated with improved fit of the truncated G–R curve over the linear G–R. Fit was estimated by calculating the χ^2 statistic for each model misfit to the FMD observations above the M_c .

Focal Mechanism. We calculated a fault-plane solution for the largest event, which was just large enough to make reliable identifications of first-motion polarities at local and nearby regional stations. We used *FocMec* to perform a grid search of the focal sphere for a double-couple solution (80) and then took the median solution with zero polarity errors. A grid-search fit is justified by previous nearby studies that found clear double-couple mechanisms along apparently preexisting basement faults (9, 10, 18, 21).

HF Well Data. Stimulation reports, drill surveys, and production data were retrieved from the ODNR online database (<https://gis.ohiodnr.gov/MapViewer/?config=oilgaswells>). Gas and water production were reported each quarter (Fig. 6), such that wells that begin flowback near the end of a quarter will have low values in their first quarter despite daily flowback being largest initially and decreasing over time.

ACKNOWLEDGMENTS. This research benefited from discussions with D. Eaton, R. Schultz, J. Shemeta, and T. Tyrrell. Seismic data were obtained from the Incorporated Research Institutions for Seismology (IRIS) Data Management Center (www.iris.edu) and ODNR. Plots were made using Generic Mapping Tools v.4.2.1 (www.soest.hawaii.edu/gmt/). Support was provided by NSF Grant 1614942, US Geological Survey National Earthquake Hazards Reduction Program Grant G15AP00089, a Kosciuszko Foundation Grant for year 2016/2017, and the ODNR Geologic Survey. Any use of trade, firm, or product names is for descriptive purposes only and does not imply endorsement by the US Government.

1. National Academy of Sciences (NAS) (2012) *Induced Seismicity Potential in Energy Technologies* (Natl Acad Press, Washington, DC).
2. Ellsworth WL (2013) Injection-induced earthquakes. *Science* 341:1225–1229.
3. McGarr A, et al. (2015) Geophysics. Coping with earthquakes induced by fluid injection. *Science* 347:830–831.
4. Weingarten M, Ge S, Godt JW, Bekins BA, Rubinstein JL (2015) INDUCED SEISMICITY. High-rate injection is associated with the increase in U.S. mid-continent seismicity. *Science* 348:1336–1340.
5. Petersen MD, et al. (2016) 2016 One-Year Seismic Hazard Forecast for the Central and Eastern United States from Induced and Natural Earthquakes (US Geological Survey, Denver, CO), Open-File Report 2016–1035.
6. Rubinstein JL, Mahani AB (2015) Myths and facts on wastewater injection, hydraulic fracturing, enhanced oil recovery, and induced seismicity. *Seismol Res Lett* 86:1060–1067.

7. Holland A (2013) Earthquakes triggered by hydraulic fracturing in south-central Oklahoma. *Bull Seismol Soc Am* 103:1784–1792.
8. Clarke H, Eisner L, Styles P, Turner P (2014) Felt seismicity associated with shale gas hydraulic fracturing: The first documented example in Europe. *Geophys Res Lett* 41:8308–8314.
9. Skoumal RJ, Brudzinski MR, Currie BS (2015a) Induced earthquakes during hydraulic fracturing in Poland Township, Ohio. *Bull Seismol Soc Am* 105:189–197.
10. Skoumal RJ, Brudzinski MR, Currie BS (2015c) Distinguishing induced seismicity from natural seismicity in Ohio: Demonstrating the utility of waveform template matching. *J Geophys Res Solid Earth* 120:6284–6296.
11. Atkinson GM, et al. (2016) Hydraulic fracturing and seismicity in the western Canada sedimentary basin. *Seismol Res Lett* 87:631–647.
12. Shapiro SA, Dinske C (2009) Fluid-induced seismicity: Pressure diffusion and hydraulic fracturing. *Geophys Prospect* 57:301–310.

13. Segall P, Lu S (2015) Injection-induced seismicity: Poroelastic and earthquake nucleation effects. *J Geophys Res Solid Earth* 120:5082–5103.
14. Deng K, Liu Y, Harrington RM (2016) Poroelastic stress triggering of the December 2013 Crooked Lake, Alberta, induced seismicity sequence. *Geophys Res Lett* 43: 8482–8491.
15. Goebel TH, Weingarten M, Chen X, Haffener J, Brodsky EE (2017) The 2016 Mw5.1 Fareview, Oklahoma earthquakes: Evidence for long-range poroelastic triggering at >40 km from fluid disposal wells. *Earth Planet Sci Lett* 472:50–61.
16. Barbour AJ, Norbeck JH, Rubinstein JL (2017) The effects of varying injection rates in Osage County, Oklahoma, on the 2016 Mw 5.8 Pawnee earthquake. *Seismol Res Lett* 88:1040–1053.
17. Lele SP, Tyrrell T, Dasari GR, Symington WA (2017) Geomechanical analysis of hydraulic fracturing induced seismicity at Duvernay field in western Canadian sedimentary basin. *GeoConvention 2017*. Available at https://www.geoconvention.com/archives/2017/161_GC2017_Geomechanical_Analysis_of_Hydraulic_Fracturing_Induced_Seismicity.pdf. Accessed August 30, 2017.
18. Kim W-Y (2013) Induced seismicity associated with fluid injection into a deep well in Youngstown, Ohio. *J Geophys Res Solid Earth* 118:3506–3518.
19. Skoumal RJ, Brudzinski MR, Currie BS, Levy J (2014) Optimizing multi-station earthquake template matching through re-examination of the Youngstown, Ohio sequence. *Earth Planet Sci Lett* 405:274–280.
20. Skoumal RJ, Brudzinski MR, Currie BS (2015) Microseismicity induced by deep wastewater injection in Southern Trumbull County, Ohio. *Seismol Res Lett* 86: 1326–1334.
21. Friberg PA, Besana-Ostman GM, Dricker I (2014) Characterization of an earthquake sequence triggered by hydraulic fracturing in Harrison County, Ohio. *Seismol Res Lett* 85:1295–1307.
22. Skoumal RJ, Brudzinski MR, Currie BS (2016) An efficient repeating signal detector to investigate earthquake swarms. *J Geophys Res Solid Earth* 121:5880–5897.
23. Weichert DH (1980) Estimation of the earthquake recurrence parameters for unequal observation periods for different magnitudes. *Bull Seismol Soc Am* 70:1337–1346.
24. Gutenberg B, Richter CF (1944) Frequency of earthquakes in California. *Bull Seismol Soc Am* 34:185–188.
25. Frohlich C, Davis S (1993) Teleseismic b-values: Or, much ado about 1.0. *J Geophys Res* 98:631–644.
26. Kagan YY (1999) Universality of the seismic moment-frequency relation. *Pure Appl Geophys* 155:537–574.
27. Wech A, Kenneth W, Creager C, Houston H, Vidale J (2010) An earthquake-like magnitude–frequency distribution of slow slip in northern Cascadia. *Geophys Res Lett* 37:L22310.
28. Schorlemmer D, Wiemer S, Wyss M (2005) Variations in earthquake-size distribution across different stress regimes. *Nature* 437:539–542.
29. Bachmann CE, Wiemer S, Goertz-Allmann BP, Woessner J (2012) Influence of pore-pressure on the event-size distribution of induced earthquakes. *Geophys Res Lett* 39: L09302.
30. Skoumal RJ, Brudzinski MR, Currie BS (2016) Proximity of Precambrian basement affects the likelihood of induced seismicity in the Appalachian, Illinois, and Williston Basins. *2016 Southern California Earthquake Center Annual Meeting*. Available at <https://www.scec.org/publication/6570>. Accessed October 16, 2017.
31. Zhang Y, et al. (2013) Hydrogeologic controls on induced seismicity in crystalline basement rocks due to fluid injection into basal reservoirs. *Groundwater* 51:525–538.
32. Morris AP, et al. (2017) Lessons learned from the Youngstown, Ohio induced earthquake sequence January 2011 to January 2012. *J Rock Mech Geotech Eng* 9:783–796.
33. Zoback ML (1992) Stress field constraints on intraplate seismicity in eastern north America. *J Geophys Res Solid Earth* 97:11761–11782.
34. Hurd O, Zoback MD (2012) Intraplate earthquakes, regional stress and fault mechanics in the central and eastern US and southeastern Canada. *Tectonophysics* 581:182–192.
35. Baranoski MT (2013) Structure contour map on the Precambrian unconformity surface in Ohio and related basement features (Ohio Department of Natural Resources, Division of Geological Survey, Columbus, OH), Map PG-23, Version 2.0.
36. Maxwell SC, et al. (2009) Fault activation during hydraulic fracturing. *SEG Technical Program Expanded Abstracts 2009* (Society of Exploration Geophysicists, Tulsa, OK), pp 1552–1556.
37. Downie RC, Kronenberg E, Maxwell SC (2010) Using microseismic source parameters to evaluate the influence of faults on fracture treatments: A geophysical approach to interpretation. *SPE Annual Technical Conference and Exhibition* (Society of Petroleum Engineers, Richardson, TX).
38. Zhou R, Huang GD, Snelling P, Thornton MP, Mueller M (2013) Magnitude calibration for microseismic events from hydraulic fracture monitoring. *SEG Technical Program Expanded Abstracts 2013* (Society of Exploration Geophysicists, Tulsa, OK), pp 2145–2149.
39. Mousavi SM, Ogwari PO, Horton SP, Langston CA (2017) Spatio-temporal evolution of frequency-magnitude distribution and seismogenic index during initiation of induced seismicity at Guy-Greenbrier, Arkansas. *Phys Earth Planet Inter* 267:53–66.
40. Huang Y, Beroza GC (2015) Temporal variation in the magnitude-frequency distribution during the Guy-Greenbrier earthquake sequence. *Geophys Res Lett* 42: 6639–6646.
41. Caputo M (1976) Model and observed seismicity represented in a two-dimensional space. *Ann Geofis* 29:277–288.
42. Aki K (1965) Maximum likelihood estimate of b in the formula $\log N = a - bM$ and its confidence limits. *Bull Earthquake Res Inst Univ Tokyo* 43:237–239.
43. Šilény J, Hill DP, Eisner L, Cornet FH (2009) Non-double-couple mechanisms of microearthquakes induced by hydraulic fracturing. *J Geophys Res Solid Earth* 114: B08307.
44. Wolhart SL, et al. (2006) Hydraulic fracture diagnostics used to optimize development in the Jonah field. *SPE Annual Technical Conference and Exhibition* (Society of Petroleum Engineers, Richardson, TX).
45. Harding TP (1985) Seismic characteristics and identification of negative flower structures, positive flower structures, and positive structural inversion. *AAPG Bull* 69: 582–600.
46. Free JC (2017) Relationships between pre-existing structure, regional stress orientation, & seismicity induced by wastewater injection, Washington County, Ohio. BS thesis (Miami University, Oxford, OH).
47. Eaton DW, Davidsen J, Pedersen PK, Boroumand N (2014) Breakdown of the Gutenberg-Richter relation for microearthquakes induced by hydraulic fracturing: Influence of stratabound fractures. *Geophys Prospect* 62:806–818.
48. Maghsoudi S, Eaton DW, Davidsen J (2016) Nontrivial clustering of microseismicity induced by hydraulic fracturing. *Geophys Res Lett* 43:10672–10679.
49. Warpinski NR, Du J, Zimmer U (2012) Measurements of hydraulic-fracture-induced seismicity in gas shales. *SPE Prod Oper* 27:240–252.
50. Goebel THW, Kwiatek G, Becker TW, Brodsky EE, Dresen G (2017) What allows seismic events to grow big?: Insights from b-value and fault roughness analysis in laboratory stick-slip experiments. *Geology* 45:815–818.
51. Perrin C, Manighetti I, Ampuero JP, Cappa F, Gaudemer Y (2016) Location of largest earthquake slip and fast rupture controlled by along-strike change in fault structural maturity due to fault growth. *J Geophys Res Solid Earth* 121:3666–3685.
52. Savage HM, Brodsky EE (2011) Collateral damage: Evolution with displacement of fracture distribution and secondary fault strands in fault damage zones. *J Geophys Res* 116:B03405.
53. Ikari MJ, Marone C, Saffer DM (2011) On the relation between fault strength and frictional stability. *Geology* 39:83–86.
54. Mori J, Abercrombie RE (1997) Depth dependence of earthquake frequency-magnitude distributions in California: Implications for rupture initiation. *J Geophys Res* 102:15081–15090.
55. Solis MP (2016) Sinistral transpression along previously existing faults, Appalachian Basin, Ohio. *AAPG Eastern Section Meeting 2016 Abstracts* (American Association of Petroleum Geologists, Tulsa, OK), article no. 90258.
56. Clifford MJ (1973) Silurian rock salt in Ohio: Report of Investigations (Ohio Division of Geological Survey, Columbus, OH), RI 90.
57. Baranoski MT (1993) The Cambridge Monocline: A revisitation of a major positive structural inversion in southeastern Ohio. *Proceedings of the First Technical Symposium* (Ohio Geological Society, Columbus, OH), pp 1–9.
58. Root S (1996) Recurrent basement faulting and basin evolution, West Virginia and Ohio: The Burning Springs–Cambridge fault zone. *Basement and Basins of Eastern North America*, eds van der Pluijm BA, Catocinos PA (Geological Society of America, Boulder, CO), Geological Society of America Special Paper, Vol 308, pp 127–134.
59. Baranoski MT, Riley RA (2013) Analysis of stratigraphic, structural, and production relationships of Devonian shale gas reservoirs in Meigs County, Ohio (Ohio Department of Natural Resources, Division of Geological Survey, Columbus, OH), Open File Report 88-3.
60. Shapiro SA, Patzig R, Rothert E, Rindshwenter J (2003) Triggering of seismicity by pore-pressure perturbations: Permeability-related signatures of the phenomenon. *Pure Appl Geophys* 160:1051–1066.
61. Holtkamp SG, Brudzinski MR, Currie BS (2015) Remote detection and monitoring of injection-induced seismicity: Application to the 2010–12 Youngstown, Ohio seismic sequence. *AAPG Bull* 99:1671–1688.
62. Schultz R, Wang R, Gu YJ, Haug K, Atkinson G (2017) A seismological overview of the induced earthquakes in the Duvernay play near Fox Creek, Alberta. *J Geophys Res Solid Earth* 122:492–505.
63. Bao X, Eaton DW (2016) Fault activation by hydraulic fracturing in western Canada. *Science* 354:1406–1409.
64. Anderson RN (1980) Phase changes & the frequency-magnitude distribution in the upper plane of the deep seismic zone beneath Tohoku, Japan. *J Geophys Res* 85: 1389–1398.
65. Wiemer S, McNutt SR (1997) Variations in the frequency magnitude distribution with depth in two volcanic areas: Mount St Helens, Washington, and Mt Spurr, Alaska. *Geophys Res Lett* 24:189–192.
66. Lei X, Yu G, Ma S, Wen X, Wang Q (2008) Earthquakes induced by water injection at ~3 km depth within the Rongchang gas field, Chongqing, China. *J Geophys Res* 113: B10310.
67. McGarr A (2014) Maximum magnitude earthquakes induced by fluid injection. *J Geophys Res Solid Earth* 119:1008–1019.
68. Shapiro SA, Krüger OS, Dinske C, Langenbruch C (2011) Magnitudes of induced earthquakes and geometric scales of fluid-stimulated rock volume. *Geophysics* 76: 55–63.
69. Dieterich J (1994) A constitutive law for rate of earthquake production and its application to earthquake clustering. *J Geophys Res* 99:2601–2618.
70. Doser DI, Kanamori H (1986) Depth of seismicity in the imperial valley region (1977–1983) and its relationship to heat flow, crustal structure, and the October 15, 1979, earthquake. *J Geophys Res* 91:675–688.
71. Marone C, Scholz CH (1988) The depth of seismic faulting and the upper transition from stable to unstable slip regimes. *Geophys Res Lett* 15:621–624.
72. Ben-Zion Y, Lyakhovsky V (2006) Analysis of aftershocks in a lithospheric model with seismogenic zone governed by damage rheology. *Geophys J Int* 165:197–210.
73. Hagin PN, Zoback MD (2004) Viscous deformation of unconsolidated sands—Part 1: Time-dependent deformation, frequency dispersion, and attenuation. *Geophysics* 69: 731–741.
74. Sone H, Zoback MD (2014) Time-dependent deformation of shale gas reservoir rocks and its long-term effect on the in situ state of stress. *Int J Rock Mech Min Sci* 69:120–132.

75. Herrmann RB (2013) Computer programs in seismology: An evolving tool for instruction & research. *Seismol Res Lett* 84:1081–1088.
76. Waldhauser F, Ellsworth WL (2000) A double-difference earthquake location algorithm: Method & application to the northern Hayward fault, California. *Bull Seismol Soc Am* 90:1353–1368.
77. Chen W-P, Molnar P (1983) Focal depths of intracontinental and intraplate earthquakes and their implications for the thermal and mechanical properties of the lithosphere. *J Geophys Res* 88:4183–4214.
78. Bender B (1983) Maximum likelihood estimation of b values for magnitude grouped data. *Bull Seismol Soc Am* 73:831–851.
79. Wiemer S, Wyss M (2000) Minimum magnitude of completeness in earthquake catalogs: Examples from Alaska, the western United States, and Japan. *Bull Seismol Soc Am* 90:859–869.
80. Snoke JA (2003) FOCMEC: FOcal MEchanism Determinations Package. Version 6.28.03. Available at www.iris.edu/pub/programs/focmec/. Accessed February 2015.
81. Brudzinski MR, Chen W-P (2003) Visualization of seismicity along subduction zones: Toward a physical basis. *Seismol Res Lett* 74:731–738.